

# Janus effect of FeCo dual atom catalyst with Co as active center in acidic oxygen reduction reaction

Received: 6 January 2025

Accepted: 25 July 2025

Published online: 05 August 2025

Check for updates

Long-Ji Yuan<sup>1,2,7</sup>, Zhen-Yu Miao<sup>3,7</sup>, Xu-Lei Sui<sup>1,2,7</sup>✉, Chi-Feng Lee<sup>4</sup>, Qi Li<sup>1,2</sup>, Mei-Jie Yin<sup>1,2</sup>, Li-Xiao Shen<sup>1,2</sup>, Ying-Rui Lu<sup>5</sup>, Zi-Gang Zhao<sup>3,6</sup>, Yu-Zhe Liu<sup>1,2</sup>, Lin-Sheng Zhu<sup>1,2</sup>, Wei Gong<sup>1,2</sup>, Wen-Liang Feng<sup>1,2</sup>, Hsiao-Tsu Wang<sup>4</sup>✉, Guo-Xu Zhang<sup>3</sup>✉ & Zhen-Bo Wang<sup>1,2,3</sup>✉

Dual-atom catalysts (DACs) represent a frontier in heterogeneous electrocatalysis for the oxygen reduction reaction (ORR) in proton exchange membrane fuel cells. However, the dynamic evolution of active-site structure complicates mechanistic understanding. Herein, alloyed Fe-Co DACs with strong Fe-Co bonds are synthesized via molecular chelation and ionic coupling strategies. In-situ spectroscopy combined with theoretical calculation reveals the Janus effect of Fe-Co dual-atom sites: Co serves as the primary catalytic center for the 4e<sup>-</sup> process with Fe as the cooperative sites to absorb the \*OH. This division-of-labor mechanism lowers the theoretical overpotential from 1.14 V to 0.43 V for acidic oxygen reduction reaction. Thus, the catalyst achieves a 0.852 V half-wave potential and 1.14 W cm<sup>-2</sup> power density (2.0 bar H<sub>2</sub>-O<sub>2</sub>), sustaining 81% peak power after 10,000 cycles. These findings clarify DAC configuration-mechanism relationships, guiding the design of high-performance DACs.

Dual-atom catalysts (DACs), which are composed of transition metal atom pairs (Fe, Co, Mn, Cu, Ni, etc.) in homonuclear or heteronuclear ways, have emerged as a transformative advancement and become an alternative to single-atom catalysts (SACs) and classic nano-cluster catalysts, which offer enhanced potential in the heterogeneous catalysis field<sup>1,2</sup>. Just like the SACs, DACs have the potential to surge atom utilization to its fullest extent, reaching a 100% efficiency, and facilitate an in-depth examination of the dynamic mechanisms of the electrons and atoms involved in the catalytic reaction<sup>3,4</sup>. This atomistic understanding establishes fundamental theoretical frameworks for designing and preparing highly effective catalysts<sup>5</sup>. Admittedly, based on their specific electronic and geometric properties due to the two main

centers, DACs have shown extremely superior catalytic performance in extensive catalytic reactions, such as oxygen evolution reaction, carbon dioxide reduction reaction (CO<sub>2</sub>RR), nitrogen reduction reaction, and oxygen reduction reaction (ORR)<sup>6–9</sup>. Meanwhile, the merits of DACs are obvious in the heterogeneous catalysts process. With the extended engineering space of active sites, DACs can easily break the scaling relation limitations and exploit the activity based on the synergistic effect, which is almost scarcely possible in the SACs.

So far, a large amount of research has been conducted on DACs, especially for the Fe-based DACs, as it has been proven to have a huge potential to replace the platinum-based catalysts in ORR, especially for the proton exchange membrane fuel cells (PEMFCs) with lower carbon

<sup>1</sup>College of Materials Science and Engineering, Shenzhen University, Shenzhen, Guangdong, PR China. <sup>2</sup>Guangdong Provincial Key Laboratory of New Energy Materials Service Safety, Shenzhen University, Shenzhen, Guangdong, PR China. <sup>3</sup>School of Chemistry and Chemical Engineering, Harbin Institute of Technology, Harbin, Heilongjiang, PR China. <sup>4</sup>Bachelor's Program in Advanced Materials Science, Tamkang University, New Taipei, Taiwan, ROC. <sup>5</sup>National Synchrotron Radiation Research Center, Hsinchu Science Park, Hsinchu, Taiwan, ROC. <sup>6</sup>College of Materials Science and Chemical Engineering, Harbin Engineering University, Harbin, Heilongjiang, PR China. <sup>7</sup>These authors contributed equally: Long-Ji Yuan, Zhen-Yu Miao, Xu-Lei Sui.

✉ e-mail: [suixulei@szu.edu.cn](mailto:suixulei@szu.edu.cn); [htwang@mail.tku.edu.tw](mailto:htwang@mail.tku.edu.tw); [zhanggx@hit.edu.cn](mailto:zhanggx@hit.edu.cn); [wangzhenbo@szu.edu.cn](mailto:wangzhenbo@szu.edu.cn)

emission, and clean and renewable characteristics. Significant progress has been made in this field<sup>10,11</sup>. Studies have shown that the type of the second metal significantly impacts the ORR performance of Fe-based DACs<sup>12–15</sup>. The addition of another metal atom will form a dual-atom structure with typical Janus structure characteristics. This Janus dual-atom structure enables the dual atoms to play completely different roles during the catalytic process, thus generating a typical effect with Janus characteristics, namely the Janus effect<sup>16</sup>. The Janus effect originates primarily from heteronuclear configurations with asymmetric electronic structures and bidirectional charge transfer between distinct metal centers, which enables differentiated adsorption/activation behaviors for diverse reaction intermediates. Various heteronuclear Fe-based DACs, such as the Fe-Cu, Fe-Ru, Fe-Mn, and Fe-Co, have been reported to alter the electronic structure of the active centers or exhibit synergistic catalysis through the Janus effect<sup>17–20</sup>. According to the Sabatier principle<sup>21</sup>, an optimal catalytic process requires a balanced interaction between the catalyst and reaction intermediates, which should be neither excessively strong nor weak. Among various transition metals (TM), Co exhibits satisfied catalytic activity as catalytic active centers second only to Fe in the ORR process, owing to its inherent suitability for interacting with O 2p orbitals<sup>22</sup>. And Fe and Co have very similar electronic orbital structures. Recent studies reveal that Fe-Co diatomic configurations demonstrate enhanced catalytic activity while maintaining stability, which suggests the existence of an intriguing Janus effect between Fe and Co<sup>23</sup>. Specifically, the Co atom is proposed to alleviate the localized d-band electrons of the Fe center, thereby mitigating the overly strong adsorption energy and optimizing the catalytic performance<sup>24,25</sup>. This self-consistent atomic adjacency facilitates the manifestation of their specific catalytic functionalities, especially for the stability requirement of non-noble catalysts in PEMFCs. Thus, the research about Fe-Co DACs is a frontier hotspot in the non-noble catalytic fields.

Although the Fe-Co DACs have shown a comparatively satisfactory catalytic performance to replace the Pt-based catalysts in PEMFCs<sup>25,26</sup>, the complexity of coordination structures has made it challenging to develop a clear approach for preparing high-performance Fe-Co DACs. Different synthesis methods for DACs have been developed, among which the pre-coordination strategy of bimetallic precursors is the most effective method for achieving a high proportion of DACs<sup>16,27,28</sup>. In addition, it still remains a great challenge to reveal the catalytic mechanism of the Janus effect in the ORR catalytic process for the Fe-Co DACs. Unlike SACs, which rely on a single catalytic center for the entire catalytic process, DACs offer more possibilities in the catalytic pathways owing to a larger number of coordination configurations and more complex interactions with intermediates<sup>29</sup>. For example, five different types of models for Fe-Co DACs have been shown in Cheng's work with the theoretical calculation, which presents vast differences in catalytic activity<sup>30</sup>. More notably, even for the same model, different catalytic pathways can be implemented and exhibit significantly different energy barriers<sup>31</sup>. So complex structural characteristics and catalytic pathways make it difficult to accurately determine which structure of DACs has the best catalytic performance, especially for the true catalytic center. Therefore, further research is extremely needed on the real reaction mechanism of Fe-Co DACs based on more dynamic and microcosmic characteristics through the combination of in-situ techniques and theoretical calculations, especially for the Janus effect in the catalytic process. Additionally, it's extremely challenging to construct DACs with a highly consistent structure because of the abundant coordination configurations of DACs. Without a satisfactory structure, it isn't easy to match theoretical calculations with actual experimental results when revealing catalytic mechanisms. In a nutshell, there is still much debate to be investigated, particularly in the design and synthesis of DACs and the deep understanding of how DACs exhibit superior performance with the potential catalytic center through the Janus effect.

Herein, an alloyed Fe-Co dual-atom structure (T-FeCo-N-C) was synthesized using small molecule chelation strategies and direct ionic coupling between the chelates and TM. In this structure, Fe and Co atoms are present as tightly bonded pairs with the same configuration, creating strong alloyed Fe-Co interactions. As a consequence of this distinctive architectural arrangement, the T-FeCo-N-C catalysts exhibit high electrochemical activity and stability, along with superior power density in complete cell setups. Through in-situ X-ray absorption spectroscopy (XAS), in-situ infrared spectroscopy, and DFT calculations, the Janus effect in the T-FeCo-N-C was elucidated and validated, particularly concerning the catalytic pathways and changes in adsorption structures during the ORR process. The insights gained from this research are anticipated to pave the way for further developments in DACs and contribute to the broader objective of optimizing catalytic processes for energy conversion applications.

## Results

### Synthesis and structure characterizations

Based on the chelation and ionic coupling effect, a regular Fe-Co diatomic site is prepared, which increases the probability of Fe-Co site formation with a high dispersion state during the pyrolysis process<sup>32,33</sup>. Specifically, the chelation effect occurs through the covalent bonding between Fe<sup>3+</sup> centers and CN ligands derived from the decomposition of monocyanoamide. After the addition of Co<sup>2+</sup>, the Co<sup>2+</sup> and NH<sub>4</sub><sup>+</sup> ions are ionically coupled to the [Fe(CN)<sub>6</sub>]<sup>3-</sup> framework and become the NH<sub>4</sub><sup>+</sup>Co<sup>2+</sup>[Fe(CN)<sub>6</sub>]<sup>3-</sup> compound (Fig. 1a, Supplementary Fig. 1), named as (Fe<sup>3+</sup>Co<sup>2+</sup>)(CN)<sub>6</sub>. This ionic interaction arises from the electrostatic attraction between Co<sup>2+</sup> and the electronegative N atom of the CN<sup>-1</sup>, just like the Potassium Ferricyanide (K<sub>3</sub>[Fe(CN)<sub>6</sub>]). Based on the small-angle X-ray scattering (SAXS), which can distinguish the degree of colloid agglomeration or coordination configuration<sup>34,35</sup>, Fig. 1b shows the characteristics of different metal salt solutions, which confirms strong chelation coordination between Fe<sup>3+</sup> and CN<sup>-1</sup> instead of Co<sup>2+</sup> and CN<sup>-1</sup>. Clearly, a new obvious scattering peak about 0.0654 nm<sup>-1</sup> illustrated that a larger size coordination configuration was formed. Comparing their absorption wavelength and intensity in Ultraviolet and Visible Spectrum (UV-Vis), as shown in Fig. 1c, (Fe<sup>3+</sup>Co<sup>2+</sup>)(CN)<sub>6</sub> shows moderate parameters, illustrating that the Co<sup>2+</sup> coupling effect weakens the strong chelation effect of Fe<sup>3+</sup> and CN<sup>-1</sup>. Based on this bimetallic precursor of the (Fe<sup>3+</sup>Co<sup>2+</sup>)(CN)<sub>6</sub> salt solution, the conventional adsorption method is further used to synthesize the objective catalyst, namely T-FeCo-N-C, as shown in Fig. 1d. More details of the experiment can be seen in the method section of the following text. In brief, the zeolite imidazole framework (ZIF-8) was synthesized as a carrier to adsorb the (Fe<sup>3+</sup>Co<sup>2+</sup>)(CN)<sub>6</sub> solution and the T-FeCo-N-C would be obtained after the pyrolysis process. For comparison, R-FeCo-N-C, S-Fe-N-C, and S-Co-N-C were obtained by a similar method just with different metal precursors (Supplementary Fig. 2), (Fe<sup>3+</sup>)(CN)<sub>6</sub> and (Co<sup>2+</sup>)(CN)<sub>6</sub> salt solutions adsorbed respectively for R-FeCo-N-C, (Fe<sup>3+</sup>)(CN)<sub>6</sub> for S-Fe-N-C, and (Co<sup>2+</sup>)(CN)<sub>6</sub> for S-Co-N-C. As shown in Supplementary Fig. 3, the X-ray diffraction (XRD) spectrum of adsorbed samples presents new diffraction peaks compared to that of ZIF-8, demonstrating strong adherence between metal chelate precursors and ZIF-8. Additionally, no metallic diffraction peaks are detected in the obtained T-FeCo-N-C and R-FeCo-N-C catalysts prepared by pyrolysis, preliminarily proving that the Fe and Co metals are dispersed at the atomic level. The control catalyst without cyanamide shows shape diffraction metal oxide peaks (CoFe<sub>2</sub>O<sub>4</sub>, JCPDS#79-1744) and alloy peaks (Co<sub>3</sub>Fe<sub>7</sub>, JCPDS#48-1816), reaffirming the effectiveness and efficiency of cyanamide-based precise precursor tuning.

As observed in the High-Resolution Transmission Electron Microscope (HR-TEM) images of T-FeCo-N-C with different resolutions (Supplementary Fig. 4a–c), the surface of the catalyst exhibits a certain degree of indentation after the pyrolysis, which is primarily attributed to the action of single cyanamide during the pyrolysis

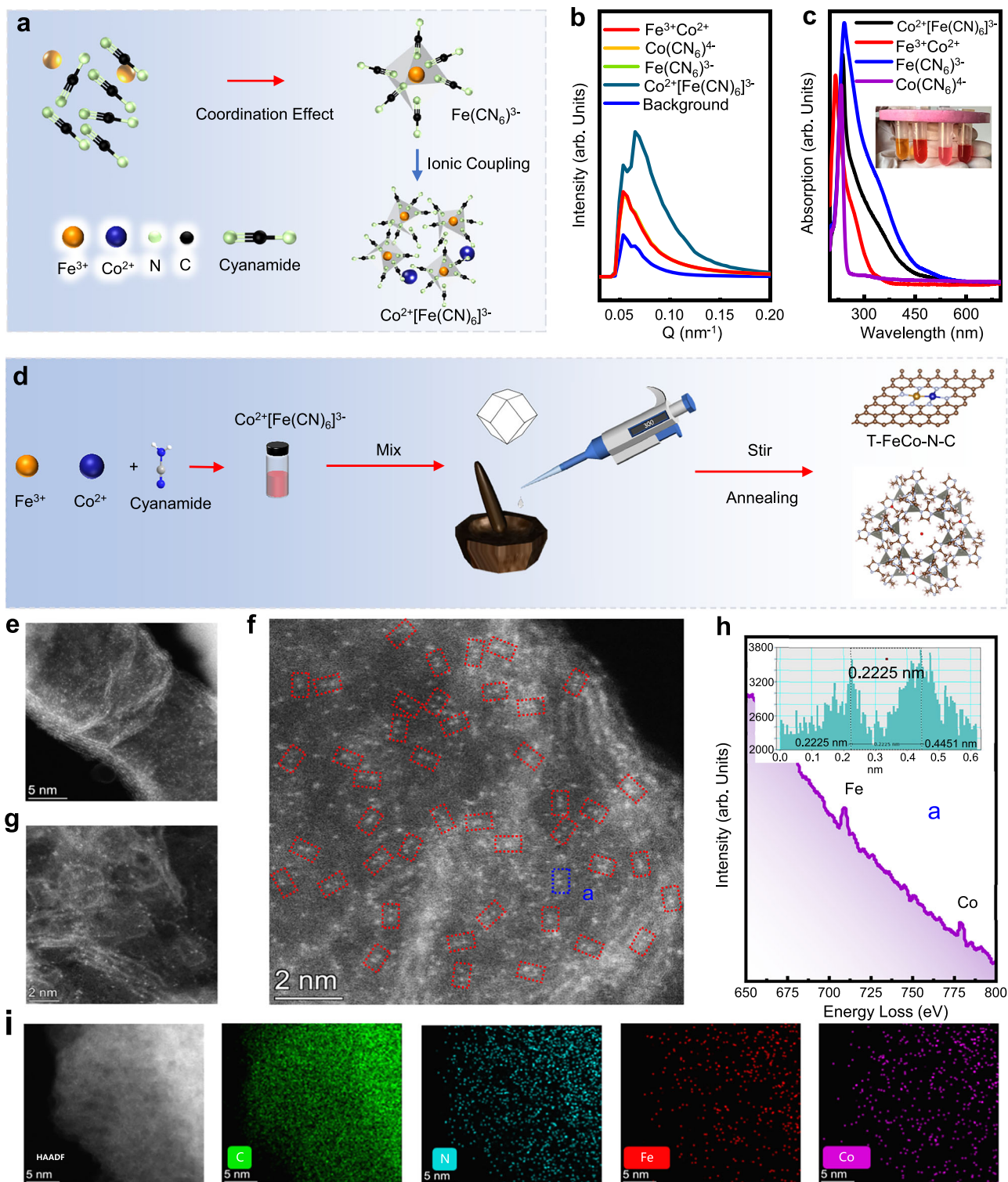


**Fig. 1 | Material synthesis and structure characterization of the T-FeCo-N-C.** **a** The Molecular chelation strategy of Fe and Co atoms. **b** SAXS peaks of solvation configurations of different metal salt. **c** UV-Vis spectra and the images of different metal salt solutions. **d** the synthesis diagram of T-FeCo-N-C. **e-g** AC-HAADF-STEM

images showing the Fe-Co diatomic sites (red rectangles) and **h** The EELS and intensity profile of Fe-Co diatomic site in the "a" area (blue rectangles in **f**). **i** HAADF-STEM image and corresponding element mappings of T-FeCo-N-C.

process. Furthermore, the HR-TEM elemental mapping in Supplementary Fig. 4d confirms the uniform distribution of all elements. The similar results for R-FeCo-N-C, S-Fe-N-C, and S-Co-N-C are shown in Supplementary Figs. 5–7. The higher of  $Area_D/Area_C$  for T-FeCo-N-C illustrates its more lattice imperfection confirmed by Raman spectra (Supplementary Fig. 8). Besides, these catalysts display a relatively

uniform porous structure without the presence of metal particles, indicating a relatively uniform atomic dispersion of Fe or Co. Brunauer-Emmett-Teller (BET) exhibits that T-FeCo-N-C has a richer pore structure, especially for the mesoporous, which further reflects that T-FeCo-N-C exhibits relatively superior mass transport capabilities (Supplementary Figs. 4, 9, and Table 1). To get more precise structure

characteristics of T-FeCo-N-C, the aberration-corrected high-angle annular dark-field scanning transmission electron microscopy (AC-HAADF-STEM) is utilized, as shown in Fig. 1e–g. Most of the metal atoms are arranged in pairs at a distance of approximately from 0.22 nm to 0.28 nm, and the percentage of metal pairs is about 62% (Supplementary Fig. 10). To further determine the composition of the atomic pairs, an electron energy loss spectroscopy (EELS) scan was performed at the positions indicated by the blue circle (Fig. 1f). The resulting EELS spectrum shown in Fig. 1h exhibits two peaks at 709.4 eV and 779.1 eV, corresponding to Fe and Co respectively, which initially confirms the presence of Fe-Co diatomic pairs. Besides, the more EELS results in different areas also illustrate the high ratio Fe-Co pairs were uniformly distributed on the T-FeCo-N-C catalysts, which illustrates the high effectiveness of the directional synthesis strategy (Supplementary Fig. 11). The elemental mapping further reveals a nearly homogeneous distribution of Fe and Co at the atomic level (Fig. 1i), and a similar element content of Fe and Co metals can be observed through the ICP-MS in Supplementary Table 2. The same content of Fe and Co (0.28 at%) indirectly illustrates the formation of the Fe-Co dual-atom structure, based on the X-ray photoelectron spectroscopy (XPS) in Supplementary Table 3. The difference in element contents in XPS and ICP-MS results is mainly because XPS is a surface test method, while ICP-MS is a volume phase test method. According to the above structural analysis, it can be concluded that Fe-Co DACs were successfully obtained based on the chelation and ionic coupling effect.

The element-specific XAS is conducted to explore the chemical states and coordination environments of T-FeCo-N-C and other samples. Based on the Co and Fe K-edge X-ray absorption near-edge structure (XANES) in Fig. 2a, b (I area), respectively, it can be observed that the absorption edge of Co and Fe in T-FeCo-N-C shift to low energy relative to those in R-FeCo-N-C, indicating that the valence states of both Co and Fe in T-FeCo-N-C are lower than in R-FeCo-N-C, and can be closed to 2+. The considerable energy shift of both Fe and Co atoms for T-FeCo-N-C illustrates a meaningful electron change, such as a strong inner electron interaction between Fe and Co atoms, due to the slight difference in the electronegativity between Co (1.88) and Fe (1.83). Besides, for the XANES spectra of Co and Fe, the pre-edge peaks near 7710 eV and 7110 eV correspond to the Co  $1s \rightarrow 3d$  and Fe  $1s \rightarrow 3d$  transitions (II area), respectively. These transitions indicate the  $D_{4h}$  symmetry distortion at the centers of both T-FeCo-N-C and R-FeCo-N-C. Moreover, the relatively higher peak intensity in T-FeCo-N-C further confirms a stronger  $D_{4h}$  symmetry distortion, primarily from the formation of the Fe-Co atomic pairs, due to a high number of unoccupied states in 3d orbital, which may mean the easier ORR process can happen in T-FeCo-N-C with the stronger  $D_{4h}$  structure. In addition, XPS was used to further analyze the chemical valence states of elements. In order to improve the signal-to-noise ratio of the XPS spectra, we increased the sample loading, prolonged the acquisition time, and enhanced the photon flux during the measurement. XPS illustrates that for the initial S-Fe-N-C catalyst,  $Fe^{3+}$  accounts for as much as 78.13% (Supplementary Fig. 12a, b and Table 4). As the Fe-Co atomic pairs increase, the proportion of  $Fe^{3+}$  gradually decreases, as evidenced by R-FeCo-N-C and T-FeCo-N-C, which are 77.52% and 62.9%, respectively. This result indicates the electron tunneling effects between Fe and Co in T-FeCo-N-C. Specifically, the interaction between the d-electrons of Fe and Co leads to the high hybridization of electron clouds due to their similar electron configuration, thereby decreasing the average valence state. In addition, it can be observed that the valences of Fe and Co for T-FeCo-N-C both decrease compared to those of S-Fe-N-C and S-Co-N-C, which can be attributed to the reduced N coordination number of Fe and Co sites. This phenomenon has been quantitatively verified through Bader charge analysis as shown in Supplementary Fig. 13. The N<sub>1</sub> and C structures for different samples are shown in Supplementary Fig. 14a, the N 1s electronic orbitals were

fitted to five different coordination environments based on high-resolution XPS spectra (specific compositions are shown in Supplementary Table 5), corresponding to pyridinic N (398.6 eV), Fe/Co-N<sub>x</sub> (399.1 eV), pyrrolic N (399.9 eV), graphitic N (401.1 eV), and oxidized N (403.3 eV)<sup>32</sup>. The Fe/Co-N<sub>x</sub> ratio in R-FeCo-N-C is 11.31%, while the Fe-N<sub>x</sub> ratio in S-Fe-N-C is 3.30%, and the Co-N<sub>x</sub> ratio in S-Co-N-C is 7.92%, which together sum to 11.22%. The rough near result of Fe/Co-N<sub>x</sub> sites further confirms that the Fe/Co-N<sub>x</sub> in the R-FeCo-N-C catalyst has less interaction between Fe and Co atoms. The lowest Fe/Co-N<sub>x</sub> ratio of 9.57% indicates that a greater number of Fe-Co bonds are formed in the T-FeCo-N-C structure, leading to an overall reduction in the Fe/Co-N<sub>x</sub> ratio. As shown in Supplementary Fig. 14b and Table 6, for S-Fe-N-C and S-Co-N-C, there is a relatively high presence of carbonates C, indicating a relatively higher degree of graphitization. In contrast, T-FeCo-N-C exhibits the lowest amount of carbonate C, suggesting that it preferentially generates a lot of defective carbon during pyrolysis. This finding aligns with the BET results, which showed a high mesopore ratio for T-FeCo-N-C.

To understand the inner coordination structures of T-FeCo-N-C, extended X-ray absorption fine structure (EXAFS), wavelet transform EXAFS (WT-EXAFS) plots, and <sup>57</sup>Fe Mössbauer transmission spectra were determined. As shown in Fig. 2c, d, the Co-N and Fe-N bonds are around 1.50 Å and 1.52 Å, respectively. The distinct peak at 2.30 Å in Fe and Co spectra can be attributed to Fe-Co bonds for T-FeCo-N-C and R-FeCo-N-C samples, which indicates the coexistence of the Fe/Co-N and Fe-Co bonds. The stronger peak of Fe-Co bonds for T-FeCo-N-C implies a higher number of Fe-Co diatom pairs, as related to R-FeCo-N-C. Additionally, the wavelet transforms (WT)-EXAFS contour plots (Fig. 2g) reveal that Co K-edge in T-FeCo-N-C exhibits two intensity maxima around 4.19 Å<sup>-1</sup> and 7.44 Å<sup>-1</sup>, corresponding to the Co-N and Co-Fe bonds. Similarly, Fe K-edge in T-FeCo-N-C displays maximum intensity around 4.47 Å<sup>-1</sup> and 7.61 Å<sup>-1</sup>, corresponding to the Fe-N and Fe-Co bonds (Fig. 2h). The Fe-Co bonds at k-space are close to the Fe foil (7.68 Å<sup>-1</sup>) and Co foil (7.20 Å<sup>-1</sup>), illustrating a strong interaction force between the Fe and Co atoms. However, for R-FeCo-N-C, the scattering intensity of the Fe-Co bond is significantly lower than that of Fe/Co-N, suggesting fewer Fe-Co diatom pairs. Considering the inherent overlap of R-space peak positions between Fe and Co backscatters in Fe-Co DACs, the fitting necessitates complementary k-space analysis (Fig. 2f). The related EXAFS fitting results of Fe and Co K-edge are shown in Supplementary Figs. 15, 16 and Tables 7, 8. For T-FeCo-N-C catalyst, the ratio of coordination numbers of Fe-N and Fe-Co are about 2.8, and the ratio of coordination numbers of Co-N and Co-Fe is about 2.9, indicating the local atomic structure of N<sub>3</sub>-Fe-Co-N<sub>3</sub>. If there are a large number of Fe or Co single-atom sites, the ratio of coordination numbers for Fe or Co would be between 3 and 4. This further demonstrates that nearly all of Fe and Co exist in the form of diatomic pairs in T-FeCo-N-C catalyst. Furthermore, the ability of Fe Mössbauer spectroscopy to distinguish different iron species stems primarily from the characteristic isomer shift (IS) and quadrupole splitting (QS) parameters, enabling high accuracy<sup>32</sup>, is used to show the inner electron structure of T-FeCo-N-C (Fig. 2e and Supplementary Table 9).

Interestingly, a sextet (six lines Zeeman splitting pattern) structure is shown in one Fe-based SAC with a ratio of 51.1%, which directly illustrates a strong electron interaction force within the inner Fe-Co bond for T-FeCo-N-C. Remarkably, the extremely low QS (0.07 mm s<sup>-1</sup>) and high magnetic hyperfine field ( $H_f$ ) (371.5 kOe) can further reflect the coordination environment. According to our knowledge, for the FeCo nano-alloy, the  $H_f$  value will increase with the decrease of nano-size and the increase in the proportion of Fe-Co alloy, suggesting a high alloying degree<sup>36–39</sup>. Thus, compared to the literature, the very high  $H_f$  value once again confirms the existence of a large number of alloyed Fe-Co bonds in T-FeCo-N-C. Additionally, just one bipolar splitting peak can be observed with a ratio of 48.9% in the fitting spectrum, showing only one type of Fe single atom with a  $D_{4h}$

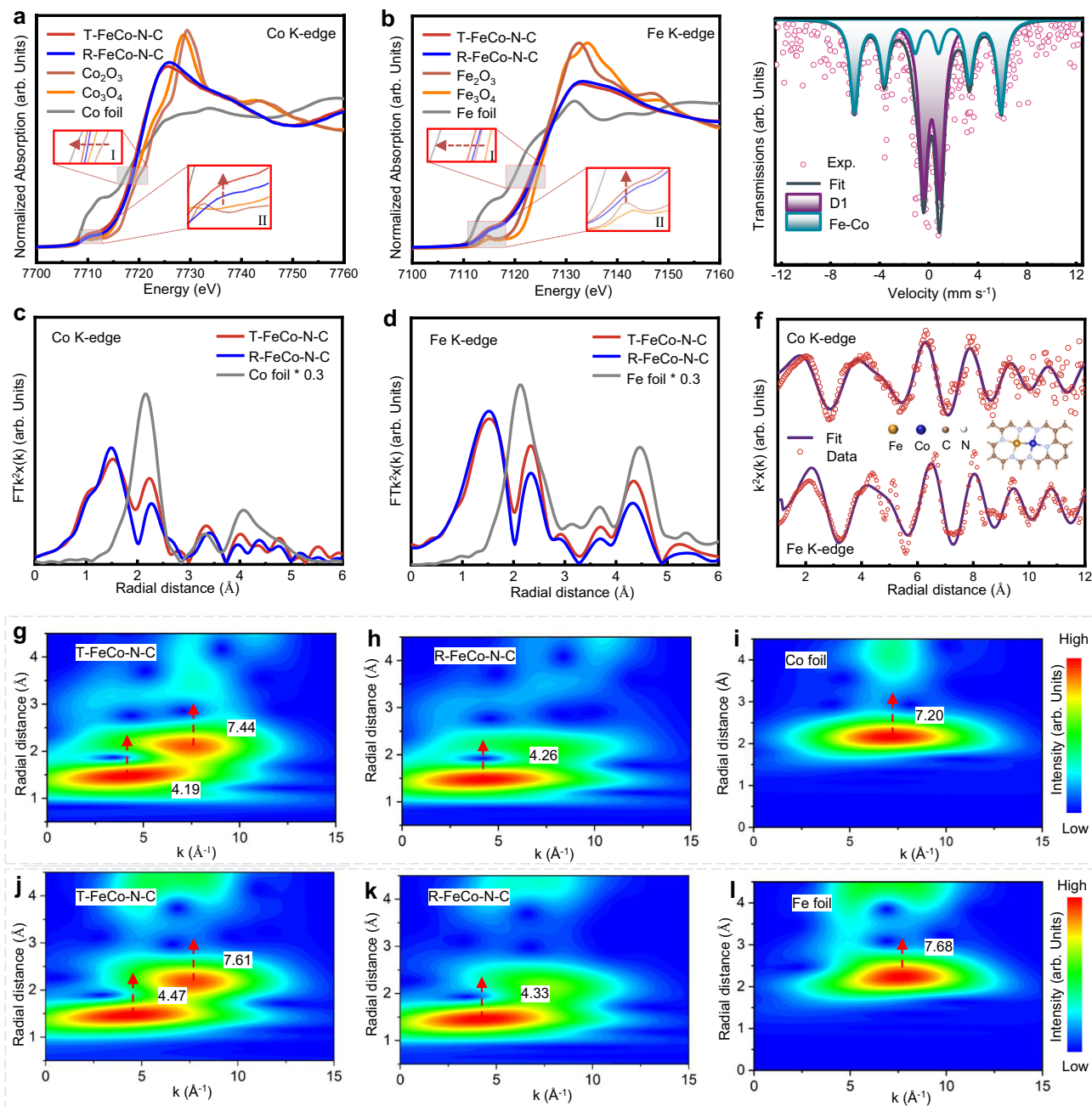


**Fig. 2 | Coordination and electron structure analysis.** **a** Ex situ Co K-edge XANES, and **b** Fe K-edge XANES of different samples.  $k^2$ -weighted Fourier transformed EXAFS spectra for the **c** Co K-edge, and **d** Fe-K-edge of different samples. **e**  $^{57}\text{Fe}$  Mössbauer transmission spectra of T-FeCo-N-C. **f** Fe and Co K-edge EXAFS (points

and fit (line) for the T-FeCo-N-C, shown in  $k$ -space of  $k^2$ -weighted, the inner Molecular model of T-FeCo-N-C. Wavelet transform of the  $k^2$ -weighted EXAFS data of **g**–**i** Co K-edge and **j**–**l** Fe K-edge for different samples.

structure. Its IS and QS values of  $-0.25$  and  $-1.33$  demonstrate the high-spin Fe in Fe-Co diatom pairs, which closely resemble the Fe-pyrrolic  $\text{N}_4$  environment, namely D1<sup>32,40</sup>. In short, all the above characterization proves that the T-FeCo-N-C catalyst has the  $\text{N}_3\text{-Fe-Co-N}_3$  configuration as the catalytic center with an extremely high number of Fe-Co diatom pairs, and the strong interaction between Fe-Co significantly affects their electronic structure.

### Electrochemical performance

The ORR performance of all catalysts was first evaluated on a rotating ring-disk electrode (RRDE) in  $\text{O}_2$ -saturated  $0.5\text{ M H}_2\text{SO}_4$  solution. The electrochemical performance of T-FeCo-N-C and R-FeCo-N-C with different Fe:Co (mass ratio) is shown in Supplementary Fig. 17a. The T-

FeCo-N-C with a Fe:Co source ratio of 3:2 shows a  $0.818\text{ V}$  half-wave potential ( $E_{1/2}$ ) versus RHE. The highest catalytic performance with this metal ratio illustrates once again the high synthesis efficiency of the pre-chelation strategy, which can reduce the disordered distribution of dual atoms during heating. An interesting result is that for R-FeCo-N-C, the half-wave potential increases progressively with increasing Fe content. When the composition is entirely Fe, the  $E_{1/2}$  reaches a maximum value of  $0.814\text{ V}$  (Supplementary Fig. 17b), suggesting that it is challenging to achieve the high-density Fe-Co atomic pairs using the Fe and Co monometallic precursors. This trend underscores the importance of pre-anchoring atomic pairs using small molecules for the formation of diatomic active centers. Besides, as shown in Supplementary Fig. 18, it can be further determined that the T-FeCo-N-C

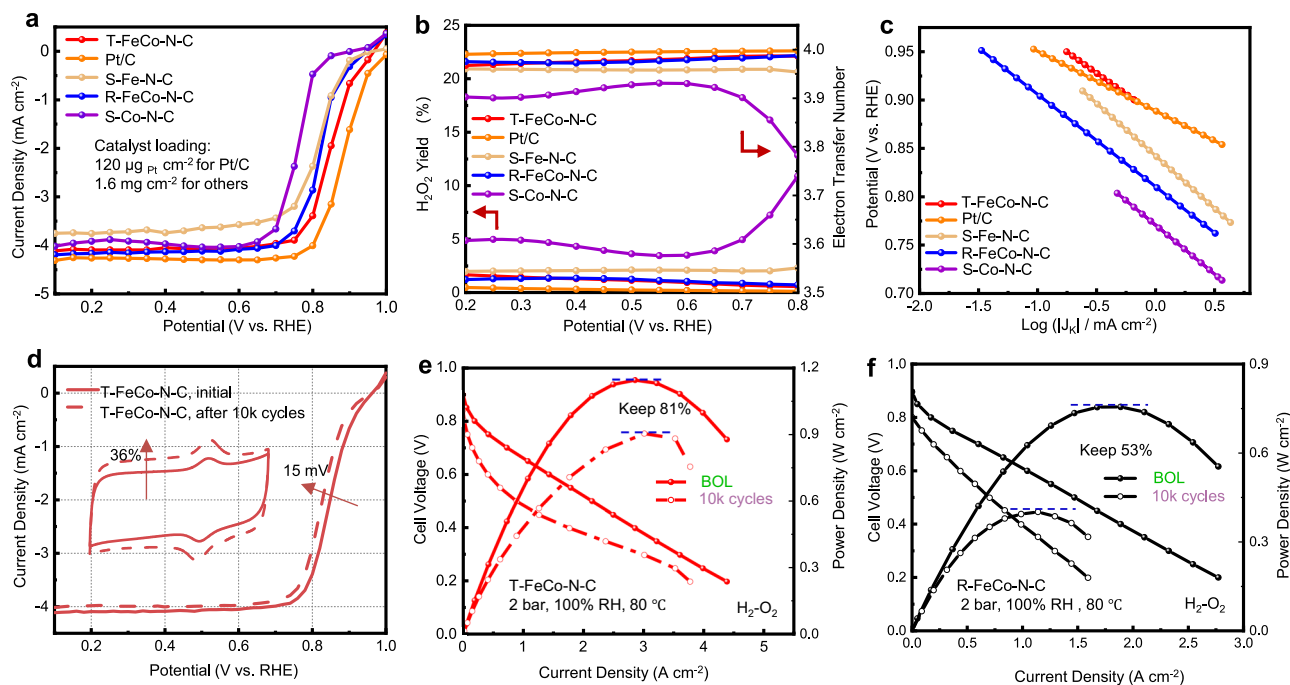


**Fig. 3 | Electrocatalytic ORR performance in acid media.** **a** ORR polarization curves for different samples in  $\text{O}_2$ -saturated 0.5 M  $\text{H}_2\text{SO}_4$  electrolyte at 25 °C under a 900 r.p.m rotation rate. A commercial 40% Pt/C catalyst ( $120 \mu\text{g}_{\text{Pt}} \text{cm}^{-2}$ ) served as the benchmark for comparison. **b**  $\text{H}_2\text{O}_2$  yields and electron transfer numbers of T-FeCo-N-C and references. **c** Tafel polarization slope for the different samples. **d** ORR polarization curves of T-FeCo-N-C in  $\text{O}_2$ -saturated and voltammetry curves

of T-FeCo-N-C in  $\text{N}_2$ -saturated (inset) before and after 10k cycles (0.6–1.0 V vs. RHE) in 0.5 M  $\text{H}_2\text{SO}_4$ . Polarization and power density curves of **e** T-FeCo-N-C, and **f** R-FeCo-N-C catalysts (Beginning of Life (BOL) and after 10k cycles AST) in  $\text{H}_2/\text{O}_2$  atmosphere under 2 bar at 80 °C as cathode materials (The flow rate was 0.5 L  $\text{min}^{-1}$  for  $\text{H}_2$ , 0.5 L  $\text{min}^{-1}$  for  $\text{O}_2$ , and the performance without IR-corrected).

catalyst exhibits optimal catalytic activity at 1050 °C. The catalyst loading for different samples has also been optimized as shown in Supplementary Fig. 19. After the above research, the T-FeCo-N-C catalysts exhibit the highest catalytic activity up to 0.852 V (Fig. 3a), which is one of the advanced reported ORR catalysts, which are shown in Supplementary Table 10 and Fig. 3g. As a comparison, the  $E_{1/2}$  of R-FeCo-N-C, S-Fe-N-C, and S-Co-N-C catalysts are only 0.825 V, 0.819 V, and 0.762 V, respectively. Meanwhile, the T-FeCo-N-C catalyst shows a similar electrochemical active area ( $22.3 \text{ mF cm}^{-2}$ ) compared to the R-FeCo-N-C ( $21.7 \text{ mF cm}^{-2}$ ), S-Fe-N-C ( $22.5 \text{ mF cm}^{-2}$ ), and S-Co-N-C ( $26.9 \text{ mF cm}^{-2}$ ), which illustrates the highest intrinsic catalytic activity in T-FeCo-N-C (Supplementary Fig. 20). The result means more Fe-Co atomic pairs can improve the catalytic performance through the Janus effect. Moreover, the ORR kinetic current density ( $j_k$ ) of T-FeCo-N-C at 0.8 V is approximately  $21.35 \text{ mA cm}^{-2}$ , significantly surpassing that of S-Fe-N-C ( $j_k = 6.25 \text{ mA cm}^{-2}$ ). At 0.85 V, the  $j_k$  of T-FeCo-N-C is about  $3.82 \text{ mA cm}^{-2}$ , which is 3.32 times greater than that of the S-Fe-N-C catalyst ( $j_k = 1.15 \text{ mA cm}^{-2}$ ), successfully demonstrating a  $1 + 1 \gg 2$  effect in catalytic activity (Supplementary Fig. 21). As shown in Fig. 3 b and Supplementary Fig. 22, the T-FeCo-N-C exhibits high selectivity with an extra low  $\text{H}_2\text{O}_2$  yield (<2.5%) and electron transfer number ( $n$ ) close to 4 over the potential range from 0.8 to 0.2 V, indicating a high selectivity for the four-electron reaction process. Meanwhile, in Fig. 3c, the Tafel slopes of T-FeCo-N-C ( $86.95 \text{ mV dec}^{-1}$ ) compared with those of R-FeCo-N-C ( $95.51 \text{ mV dec}^{-1}$ ), S-Fe-N-C ( $108.55 \text{ mV dec}^{-1}$ ), S-Co-N-C ( $101.33 \text{ mV dec}^{-1}$ ), and Pt/C ( $97.98 \text{ mV dec}^{-1}$ ) further evidence that less energy is needed to finish the ORR process of T-FeCo-N-C. Thus, both experimental and calculation results show that T-FeCo-N-C efficiently completes the ORR process to the 4-electron kinetic reaction pathway. Furthermore, long-term stability tests were carried out for T-FeCo-N-C, Pt/C, and R-FeCo-N-C catalysts, as shown in Fig. 3d and Supplementary Fig. 23. After 10,000 cycles of accelerated degradation testing (ADT), the Pt/C and R-FeCo-N-C catalysts experience a

significant loss of 35 mV and 30 mV in  $E_{1/2}$ , respectively. In contrast, the T-FeCo-N-C catalyst only shows a 15 mV loss. This result suggests that the Fe-Co atomic active centers do not undergo significant changes. Additionally, it is noteworthy that the cyclic voltammetry (CV) curve area of T-FeCo-N-C increased by 36%. This increase is primarily attributed to the corrosion of carbon substrate, which also suggests that the attenuation activity mainly comes from the substrate corrosion, rather than the destruction of the Fe-Co active structure.

To further investigate the practicality of the catalysts, the membrane electrode assemblies (MEA) performance of T-FeCo-N-C and R-FeCo-N-C under different environments were tested and shown in Fig. 3e, f, respectively. Under  $\text{H}_2/\text{O}_2$  at a pressure of 2.0 bar, T-FeCo-N-C and R-FeCo-N-C exhibit maximum power densities ( $P_{\text{max}}$ ) of up to  $1140 \text{ mW cm}^{-2}$  and  $755 \text{ mW cm}^{-2}$ , respectively, which is similar to the precious Pt/C catalysts (Supplementary Fig. 24). In an  $\text{H}_2/\text{Air}$  environment, T-FeCo-N-C also shows a high  $P_{\text{max}}$  of  $624 \text{ mW cm}^{-2}$ , surpassing the R-FeCo-N-C of  $518 \text{ mW cm}^{-2}$  (Supplementary Fig. S25). Benefiting from the strong Fe-Co construction, after accelerated square wave voltage cycling (ASTs) from 0.6 V (3 s) to 0.90 V (3 s) under  $\text{H}_2/\text{N}_2$  flows, T-FeCo-N-C delivers significantly enhanced stability, maintaining 81% of  $P_{\text{max}}$  after 10,000 cycles, while R-FeCo-N-C only keeps 53% after 10,000 cycles. More importantly, the AC-HAADF-STEM for the T-FeCo-N-C in Supplementary Fig. S26 illustrates that the structure of the catalyst has not been damaged and the diatomic centers still stably survive without the formation of any metal particles after MEA ASTs. Thus, our catalysts surpass the vast majority of reported non-precious metal catalysts (Fig. 3g, Supplementary Table 11). Considering the different proton transport and charge transfer in MEA, we further investigated the Electrochemical Impedance Spectroscopy (EIS) of T-FeCo-N-C and R-FeCo-N-C at 0.6 V (Fig. S27, Supplementary Table 12). Compared to R-FeCo-N-C, the T-FeCo-N-C had a much lower Ohmic internal resistance ( $R_{\Omega}$ ) and mass transfer resistance ( $R_{\text{mt}}$ ) in  $\text{H}_2/\text{O}_2$ . More remarkably, for the charge transfer resistance ( $R_{\text{ct}}$ ), T-FeCo-N-C

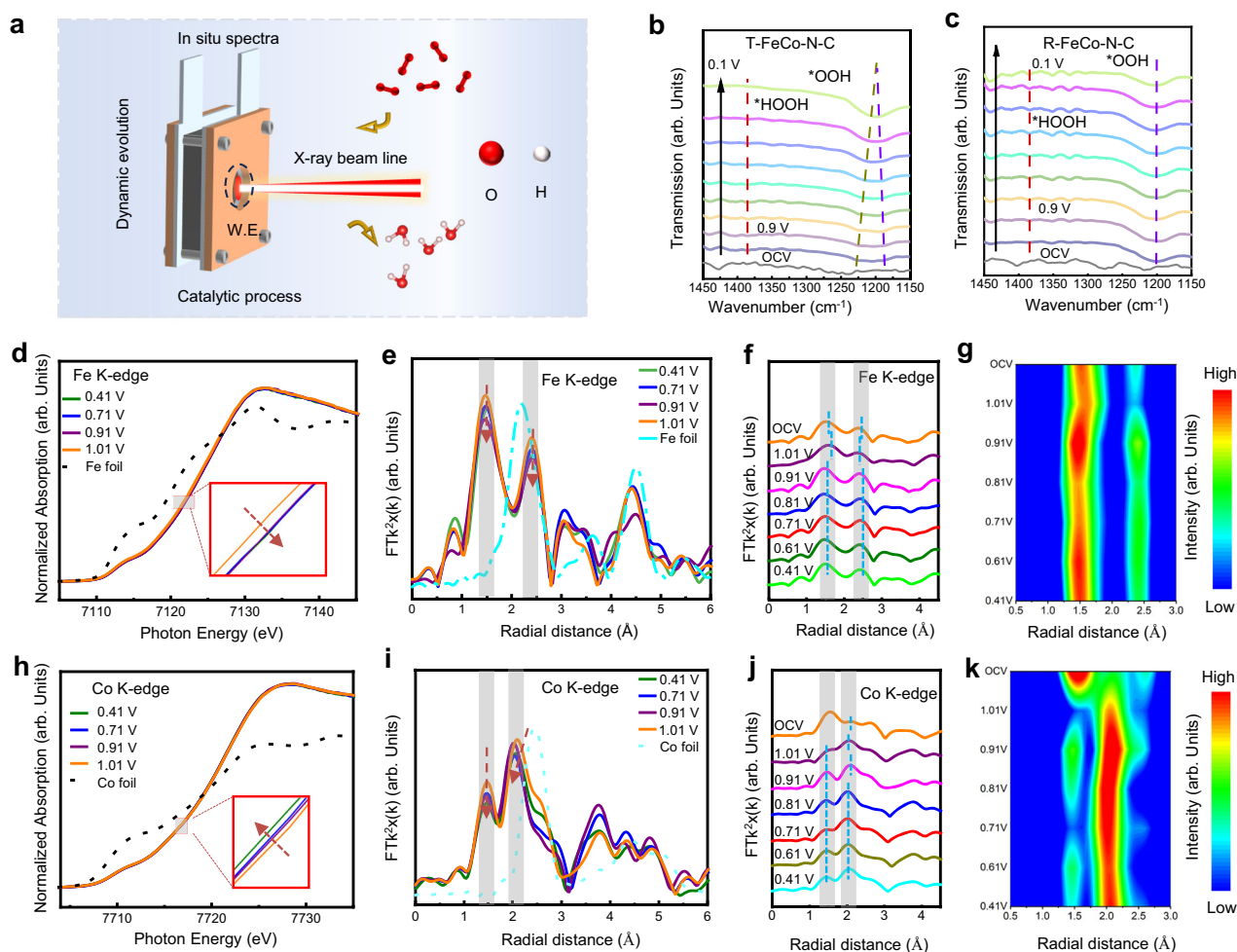


**Fig. 4 | Catalytic process study through in-situ spectrum.** **a** Schematic of the in-situ spectra setup and the inner information in the catalytic process. In-situ ATR-SEIRAS spectra on **b** T-FeCo-N-C and **c** R-FeCo-N-C. The above in-situ spectra were obtained at various potentials during ORR catalysis in  $O_2$ -saturated 0.5 M  $H_2SO_4$ .

**d** Fe K-edge and **h** Co K-edge XANES spectra of T-FeCo-N-C. **e–g** Fe K-edge EXAFS spectra and **i–k** Co K-edge EXAFS spectra of T-FeCo-N-C (the change of bond length and intensity shown in the shadow area).

exhibits a decrease of an order of magnitude compared to the R-FeCo-N-C, indicating the superior intrinsic catalytic activity. Thus, the T-FeCo-N-C with high-density Fe-Co diatomic pairs exhibits satisfactory catalytic performance in the RRDE or MEA test.

### Insight into catalytic mechanism

To understand the uniqueness of the alloyed Fe-Co DACs, the in-situ attenuated total reflection surface-enhanced infrared absorption spectroscopy (ATR-SEIRAS) and in-situ synchrotron-based XAS techniques were investigated to obtain the exact dynamic evolution of the local structure and reveal the catalytic mechanism clearly (Fig. 4a, and Supplementary Fig. 28). The in-situ ATR-SEIRAS spectra of T-FeCo-N-C firstly exhibit two different \*OOH adsorption peaks (Fig. 4b), illustrating the existence of two types of \*OOH adsorption structures on the surface of T-FeCo-N-C in the process of ORR. More interestingly, one of the \*OOH adsorption peaks shows a significant red shift from  $1225.9\text{ cm}^{-1}$  to  $1206.4\text{ cm}^{-1}$  as the potential decreases, while the other hardly changes. This phenomenon may indicate that the \*OOH adsorption structure with a significant red shift is a highly active structure with faster reaction kinetics, and the other one is exactly the opposite. In sharp contrast to T-FeCo-N-C, as shown in Fig. 4c, there is only one \*OOH adsorption peak for R-FeCo-N-C, and it has no shift as the potential decreases. It indicates that there is only one relatively stable \*OOH adsorption structure on the surface of R-FeCo-N-C with

slower reaction kinetics. In addition, the in-situ signal intensity of T-FeCo-N-C catalyst has a more significant change at various potentials than that of R-FeCo-N-C catalyst. This further highlights the superior kinetic characteristics of T-FeCo-N-C catalyst. All the results demonstrate that for the alloyed Fe-Co DACs, there are two reaction pathways simultaneously present in the ORR process, and one of them has a lower energy barrier as the main reaction pathway.

In order to reveal the Janus effect of Fe-Co atomic pairs and disclose the unique results for \*OOH in the ATR-SEIRAS during the catalytic process, the chemical valence states and coordination structures of Fe and Co in T-FeCo-N-C were detected at different potentials by in-situ XAS<sup>17</sup>. The Fe and Co K-edge XANES and EXAFS spectra of T-FeCo-N-C at different potentials from the open-circuit voltage (OCV), 1.01 V, 0.91 V to 0.41 V vs. RHE are displayed in Fig. 4d–k. From the XANES of Fe K-edge and Co K-edge, the  $D_{4h}$  structure has little change during the catalytic process (Fig. 4d, h), which means that a stable alloyed Fe-Co catalytic center in the T-FeCo-N-C<sup>16,41</sup>. A notable observation is that the Fe-Co bond lengths appear different, approximately 2.4 Å for the Fe K-edge and 2.1 Å for the Co K-edge, respectively. In particular, the Co-Fe bond length in the EXAFS of Co K-edge shows a clear peak shift with the decrease of potential in Fig. 4i. The shortened Co-Fe bond length enables the intensity of the Co-Fe bond to increase according to the electron backscattering enhancement effect in EXAFS theory<sup>42</sup>. In addition, the intensity of the Co-N bond is less than that of the Co-Fe

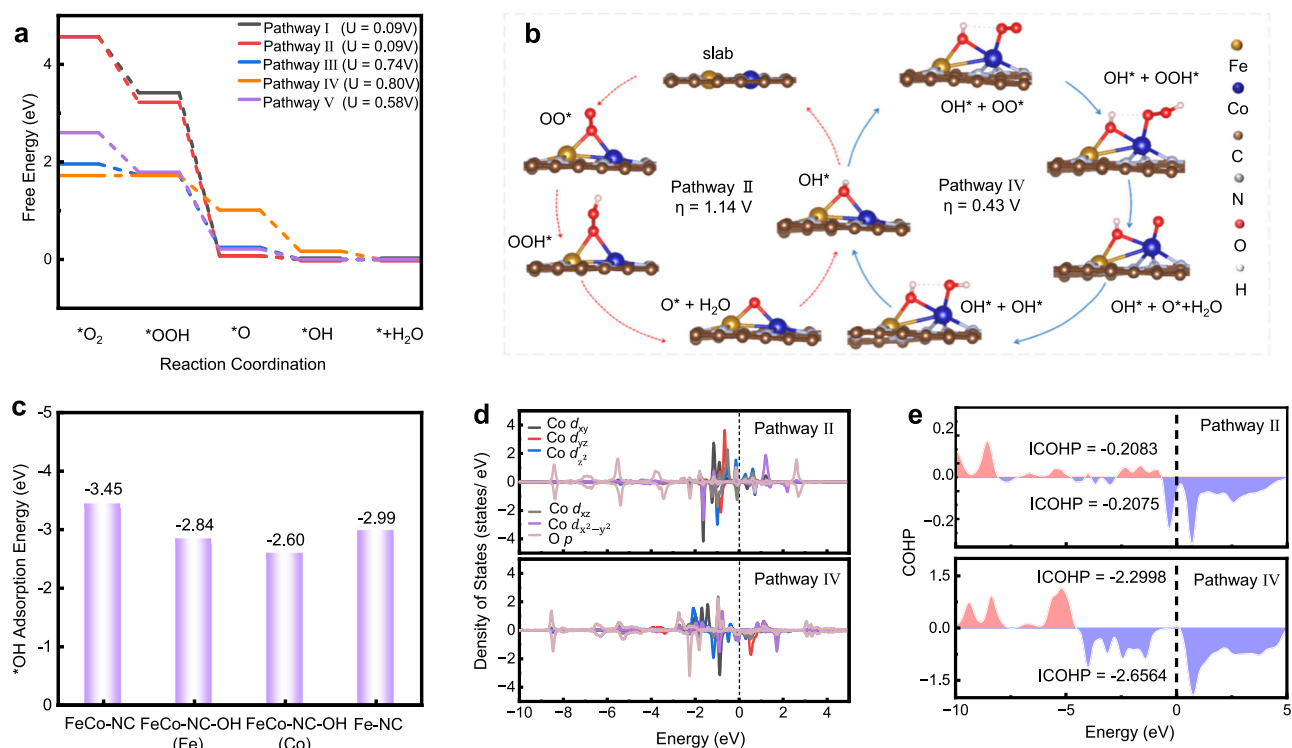


**Fig. 5 | Catalytic mechanism insights through theoretical calculation.**

**a** The ORR free energy diagrams of five different pathways considered here, for the Fe-NC, FeCo-NC, and FeCo-NC-OH catalysts. **b** A comparison of Pathway II (FeCo-NC) and Pathway IV (FeCo-NC-OH). **c** The adsorption energies of OH on top of

different catalysts. **d** Calculated projected density of states (PDOS) for the rate-determining step of Pathway II and Pathway IV. **e** Crystal orbital Hamiltonian analysis of Co-O bond after  $^*OOH$  adsorption for the Pathway II and Pathway IV with different spin states.

during the ORR process, which differs from the initial state (at OCV, Fig. 4j). In contrast, this phenomenon is not observed in the Fe K-edge (Fig. 4e). This discrepancy indicates that Co atoms have a more concentrated surrounding charge density and more obvious electronic cloud rearrangement during the catalytic process. It can be inferred that the Co atom in alloyed Fe-Co atomic pairs is likely to serve as the primary active center, which leads to the fast accumulation of catalytic intermediates in the electrical double layer of Co surface. The coverage of reaction intermediates on Co surface reduces the scattering signal intensity of the Co-N and shortens the Co-Fe bond length. This discrepancy indicates that Co atoms have a more concentrated surrounding charge density and more obvious electronic cloud rearrangement during the catalytic process. It can be inferred that the Co atom in alloyed Fe-Co atomic pairs is likely to serve as the primary active center.

To be more specific, in Fig. 4d, the absorption edge of Fe K-edge is shifted to high energy with the potential from 1.01 V to 0.91 V, and then no change is shown with the potential decrease from 0.91 V to 0.41 V, which indicates that Fe atom can easily form a stable adsorption structure at a low polarization level, and this structure remains stable even at a high polarization level. In contrast, the absorption edge of the Co K-edge presents a continuous and smooth shift to low energy with the decrease of potential as shown in Fig. 4h, which is similar to the change for the single-atom center in SACs, indicating that the Co atom remains in an active state throughout the catalytic reaction process, continuously undergoing adsorption and desorption with the intermediate products<sup>40</sup>. A similar phenomenon is shown in the EXAFS of Fe and Co K-edge in Fig. 4f, g and Fig. 4j, k. All the results again confirm that the Co atom is the main active center rather than the Fe atom. This inference is also consistent with the conclusion of the in-situ ATR-SEIRAS spectra mentioned above. It can be concluded that the reaction process leads to the formation of a stable adsorption structure on the

Fe atom. Thus, this reaction pathway with the Fe atom as the active site shows slow reaction kinetics. However, the stable adsorption structure on the Fe atom further regulates the electronic structure of Co and accelerates the other reaction process with the Co atom as the active site, delivering a new reaction pathway with fast reaction kinetics. Through this Janus effect of Fe-Co atomic pairs, the T-FeCo-N-C exhibits superior ORR performance, especially for the Co-based catalysts.

### Catalytic mechanism insights through theoretical calculation

The DFT calculations were further carried out to explore the intrinsic catalytic mechanism of the Janus effect for alloyed Fe-Co active centers. Based on the above in-situ experiment results, the Janus effect exists in the alloyed Fe-Co atomic pairs, where the Co atom serves as the main active center and the Fe atom forms a stable adsorption structure. Considering the high adsorption energy between Fe and  $^*OH$  according to the previous work, FeCo-NC catalysts with/without the OH ligand are simulated, denoted as FeCo-NC-OH, and FeCo-NC, respectively, and their slab models and geometrical parameters are shown in Supplementary Fig. 29 and Tables 13–15 (defined as pathway I–V, the atomic coordinates of the optimized computational models shown in Supplementary Data 1). We start by considering the FeCo-NC catalysts without the OH ligand, and two different  $O_2$  adsorption configurations were compared, i.e., the side-on adsorption model (pathway I) and the vertical adsorption model (pathway II). From our calculated DFT results, it can be seen that both of pathways I and II exhibit a high overpotential of 1.14 V in Fig. 5a and Supplementary Table 17, which is much inferior to the Fe-NC catalyst ( $\eta = 0.65$  V) and Co-NC catalyst ( $\eta = 0.54$  V) (Supplementary Figs. 30–31). It is mainly because of the higher energy barrier of  $^*OH$  desorption, further confirming the very stable  $^*OH$  adsorption on Fe-Co centers for FeCo-NC<sup>19</sup>. Furthermore, we investigate the dual-site dissociative pathways for FeCo-NC-OH (pathways III and IV). Pathway III refers to the catalytic

process with the Fe atom as the active center denoted as FeCo-NC-OH(Fe), whereas pathway IV corresponds to the Co active-site mode denoted as FeCo-NC-OH(Co). Both pathways III and IV show better reaction activity in comparison with pathways I and II, and the calculated overpotentials are 0.49 V and 0.43 V, respectively. It is worth noting that, among all the catalytic models, pathway IV presents the highest reaction activity, in which the Fe atom absorbs the \*OH, and the Co atom serves as the main catalytic center. This is in agreement with the chemical state change in the in-situ Fe and Co K-edge XANES results. Based on the highly self-consistent results, the Janus effect of alloyed Fe-Co active centers was further disclosed. Intuitively speaking, for pathways I and II, the rate-determining step (RDS) is confirmed as the removal of \*OH, and the computed adsorption energy of \*OH is about -3.45 eV (Fig. 5c and Supplementary Table 16), indicating a strong interaction between the Fe-Co and \*OH. However, for Pathway IV, the RDS is found to be the formation of the \*OOH, which is in agreement with another \*OOH adsorption peak in the in-situ ATR-SEIRAS (Fig. 4 b). Besides, it is worth mentioning that the adsorption energy of \*OH for FeCo-NC-OH is decreased by 0.85 eV compared to FeCo-NC (Fig. 5c). The weaker \*OH adsorption is responsible for the change of RDS from the removal of \*OH to the formation of \*OOH.

To further understand the role of the OH ligand, the geometry changes during the ORR process are analyzed. Geometry optimization was performed for all the models, and the corresponding bond lengths are tabulated in Supplementary Tables 13–15. Due to the formation of the OH ligand on the Fe atom, it is found that the interaction of Fe-N pairs is strengthened, while the Co-N bonds are weakened. When it comes to the ORR process, there is a strong charge redistribution for both pathway III and IV, which can be observed from the changes of Fe-N and Co-N bond lengths (Supplementary Table 14). The change of bond lengths in pathway IV is more consistent with the in-situ EXAFS spectra. Thus, a more probable reaction process is proposed, which is depicted in Fig. 5b, fully reflecting the Janus effect of Fe-Co active centers. In short, the Janus effect in Fe-Co DACs reconstructs the ORR pathway by leveraging the synergistic Fe-Co interaction. The Fe site strongly adsorbs \*OH, which causes the Fe site to lose its activity as a catalytic center. However, this stable structure in turn optimizes the electronic structure of the adjacent Co site, thereby activating the catalytic activity of the Co site and making Co a new high-activity center for the continuous ORR reaction.

The electronic properties were further discussed to reveal the Janus effect. Besides, the Bader charges are tabulated in Supplementary Table 18 for the Fe, Co, and O atoms during two different Pathways. It can be clearly seen that the metal active site exhibits an obvious charge variation during the ORR process while the charge of the other metal site remains basically unchanged, which also can be seen in the calculated electron density difference (EDD) result (Supplementary Fig. 32). The calculated magnetic moments of Fe and Co during the ORR process exhibit the same result in Supplementary Fig. 33. For pathway IV, the Bader charge and magnetic moment of Co atoms show clear variation, indicating the electron transfer from the Co orbitals to the related oxygenated intermediates, in good agreement with the above experiments. Furthermore, to illustrate the role of the OH ligand, the electronic properties of the configurations after \*OOH adsorption in pathways II and IV are analyzed due to \*OOH adsorption is RDS for the FeCo-NC-OH catalyst. As shown in Fig. 5d and Supplementary Figs. 34–36, the density of states (DOS) calculations demonstrate that in pathway II, the O 2p orbital of the \*OOH shows a relatively large overlapping with the  $d_{z^2}$  and  $d_{x^2-y^2}$  orbitals of Co 3d. In pathway IV, the O 2p orbital also exhibits a bonding character with the lower-energy  $d_{xz}$  orbital of Co 3d<sup>43</sup>. Moreover, the Crystal Orbital Hamiltonian Population (COHP) was computed on FeCo-NC-OH and FeCo-NC. In general, COHP provides a way of evaluating the bonding

nature, through the integration of COHP up to the Fermi level, the different orbital bonding strengths can be visualized by using the integrated COHP (ICOHP)<sup>43</sup>. Obviously, without the Fe-\*OH formation (pathways II), the extremely weak bond interaction can happen between Co catalytic center and \*OOH (ICOHP = -0.2083, and -0.2075) (Fig. 5e, Supplementary Tables 19 and 20). For pathway IV, a relatively stronger bond interaction can (ICOHP = -2.2998, -2.6564), which is consistent with the shorter bond distances of Co-O (Supplementary Tables 13 and 14). All the above results indicate that the FeCo-NC-OH catalyst shows stronger electronic interaction between Co and \*OOH than the FeCo-NC catalyst. Thus, FeCo-NC-OH can easily achieve the adsorption of \*OOH (RDS) in the ORR process. It can be concluded that the OH ligand generated from pathways I and II plays a vital role in the electronic rearrangement of Fe-Co active centers, resulting in the proper interaction with the reaction intermediates and greatly accelerating the reaction kinetics.

## Discussion

In summary, an alloyed T-FeCo-N-C catalyst with strong Fe-Co bonds was designed, and most Fe and Co atoms exist in the form of atom pairs, which have been illustrated by ICP-MS, STEM, XPS, XAS, <sup>57</sup>Fe Mössbauer spectrum. The Janus effect of Fe-Co DACs was disclosed based on the in situ characterization and theoretical calculations. Due to the very high \*OH adsorption energy, stable \*OH adsorption formed on Fe atoms optimizes the electronic structure of Co, and then Co atoms further serve as the highly active catalytic center to finish a new ORR process. Thanks to the Janus effect, the RDS of Fe-Co DACs changes from the removal of \*OH to the formation of \*OOH. Therefore, its theoretical overpotential decreases from 1.14 V to 0.43 V, exhibiting an extremely high catalytic performance of ORR. With the Co as the catalytic center, its  $E_{1/2}$  reaches a leading level of 0.852 V and exhibits a high power density of 1140 mW cm<sup>-2</sup> in an H<sub>2</sub>-O<sub>2</sub> full cell. Meanwhile, after 10,000 cycles of MEA durability testing, the maximum power density of 81% is still maintained. Based on the highly consistent in-situ experimental results and theoretical calculations, we believe this work will provide clear and convincing evidence for the Janus effect of DACs. This new, deeper viewpoint can help design DACs with satisfactory catalytic performance and understand the catalytic mechanism with a new perspective in various catalytic fields.

## Methods

### Materials

All the reagents were used directly without purification. Iron (III) nitrate nonahydrate (Fe(NO<sub>3</sub>)<sub>3</sub>·9H<sub>2</sub>O, 98%), Cobalt (II) nitrate nonahydrate (Co(NO<sub>3</sub>)<sub>3</sub>·6H<sub>2</sub>O, 98%), and 2-Methylimidazole (2-MIM, 98%) were purchased from Shanghai Aladdin Reagent Co., Ltd. Commercial Pt/C (40 wt% metal, JM) was purchased from Johnson Matthey (Shanghai) Chemicals Ltd, Zinc nitrate hexahydrate (Zn(NO<sub>3</sub>)<sub>2</sub>·6H<sub>2</sub>O, 98%) was purchased from Sinopharm Chemical Reagent Co., Ltd. Methanol (CH<sub>3</sub>OH, 99.5%), and Cyanamide (CH<sub>2</sub>N<sub>2</sub>, 95%) were purchased from Shanghai Macklin Biochemical Technology Co., Ltd.

### Preparation of ZIF-8 precursor

Typically, the ZIF-8 precursor preparation method is used in the traditional way to prepare. Firstly, 4.464 g Zn(NO<sub>3</sub>)<sub>2</sub>·6H<sub>2</sub>O was dissolved in 120 mL of methanol solution, and 4.928 g 2-MIM was added in another 120 mL of methanol solution. Subsequently, quickly mix the above-dispersed two solutions and stir for 90 min at 25 °C with 900 rpm min<sup>-1</sup> to get enough crystal nuclei. Then, the mixed liquids were allowed to stand for 22 h and 30 min at 25 °C, thus forming a nucleating homogeneous ZIF-8. The as-obtained product was centrifuged and washed with ethanol several times, and finally dried at 80 °C in a vacuum. The typical ZIF-8 precursor was obtained. (The ZIF-8 precursors in the following catalyst preparation process are stored in vacuum drying chambers when not in use.)

### Preparation of T-FeCo-N-C

Firstly, the  $[\text{Fe}^{3+}(\text{CN})_6^{-1}]_{3/x}(\text{Co}^{2+})_{2/y}$  solution be prepared. A certain amount of  $\text{Fe}(\text{NO}_3)_3 \cdot 9\text{H}_2\text{O}$  (30 mg),  $\text{Co}(\text{NO}_3)_2 \cdot 6\text{H}_2\text{O}$  (20 mg), and  $\text{CH}_2\text{N}_2$  (100 mg) were dissolved in a solvent with a 1:1 ratio of ethanol (400  $\mu\text{l}$ ) and water (400  $\mu\text{l}$ ) by volume, followed by ultrasonic at 35 °C for 30 min. Typically, 300  $\mu\text{l}$  of the above solution was dispersed into ZIF-8 (300 mg) in 6 times. By stirring well in a mortar, ZIF-8 is promoted to homogeneous adsorption, and the product is recorded as T-FeCo@ZIF-8. The loaded solid T-FeCo@ZIF-8 sample was dried in a vacuum oven for 1 h at 35 °C. Finally, the T-FeCo@ZIF-8 were placed in a tube furnace and annealed at 1050 °C for 1 h with a heating rate of 20 °C  $\text{min}^{-1}$  under flowing Ar gas and then naturally cooled to room temperature to obtain T-FeCo-N-C (The “T” means the Fe and Co metal solution together added). No additional acidic leaching and the second heating treatment were required.

### Preparation of R-FeCo-N-C

The preparation method for R-FeCo-N-C (The “R” means the Fe and Co metal solution, respectively, added without the pre-interaction in solution) is similar to the abovementioned T-FeCo-N-C, except that the metal salt solutions of Fe and Co were added in sequence, first Fe and then Co, with 50  $\mu\text{l}$  of each added in 6 separate doses, totaling 300  $\mu\text{l}$ . The Fe solution (denoted as A solution) was obtained, with only an amount of  $\text{Fe}(\text{NO}_3)_3 \cdot 9\text{H}_2\text{O}$  (30 mg), and  $\text{CH}_2\text{N}_2$  (100 mg) was dissolved in a solvent with a 1:1 ratio of ethanol (400  $\mu\text{l}$ ) and water (400  $\mu\text{l}$ ) by volume, followed by ultrasonic at 35 °C for 30 min. The Co solution (denoted as B solution) was prepared with the same process as the Fe solution, with the only difference being that  $\text{Co}(\text{NO}_3)_2 \cdot 6\text{H}_2\text{O}$  (20 mg) instead of  $\text{Fe}(\text{NO}_3)_3 \cdot 9\text{H}_2\text{O}$  (30 mg).

### Preparation of S-Fe-N-C and S-Co-N-C

The preparation methods for S-Fe-N-C and S-Co-N-C (The “S” means the Fe and Co metal solution respectively solely added) are similar to the abovementioned T-FeCo-N-C, except that the A, B solution was added instead of the  $[\text{Fe}^{3+}(\text{CN})_6^{-1}]_{3/x}(\text{Co}^{2+})_{2/y}$  solution. Meanwhile, the other material preparation process was the same.

### Morphology and structure characterizations

Electron microscopy was performed via the Merlin Compact (Carl Zeiss AG), the Tecnai G2 F30 (FEI Company), and the Themis G2 300 (FEI Company) systems. Powder X-ray diffraction (XRD) was performed using a D2 PHASER XE-T diffractometer (Bruker Corporation). High-angle annular dark field-scanning TEM (HAADF-STEM) images and elemental mapping were taken by a Thermo Fisher Scientific Spectra 300 S/TEM at 300 kV. X-ray photoelectron spectroscopy (XPS) was obtained on the ThermoFischer, ESCALAB Xi+. Among them, the vacuum degree of the analysis chamber is  $8 \times 10^{-10}$  Pa, the excitation source adopts Al K $\alpha$  ray ( $h\nu = 1486.6$  eV), the working voltage is 12.5 kV, the filament current is 16 mA, and the signal accumulation is carried out for 10 cycles. The full spectrum of the test general energy (Passing-Energy) is 100 eV, the narrow spectrum is 30 eV, the step size is 0.1 eV, the residence time is 40 - 50 ms, and the C1s = 284.80 eV binding energy is used as the energy standard for charge correction. Light spot 650 micron. Inductively coupled plasma mass spectrometry (ICP-MS) was conducted on an Agilent 7700X (Agilent Technologies). Raman spectra were obtained on Thermo Scientific DXR 2xi Micro-Raman spectrometer with semiconductor laser excitation at 785 nm.  $^{57}\text{Fe}$  Mössbauer spectra was performed using a conventional spectrometer (Germany, Wissel MS-500). Small-angle X-ray scattering (SAXS) was performed at the BL19U2 beamline of the PILATUS3 X 2 M detector at the Shanghai Synchrotron Radiation Facility (SSRF).

Ex-situ/in-situ XAFS measurements were carried out on Taiwan Photon Source's (TPS) 32A beamline of National Synchrotron Radiation Research Center (NSRRC). The Fe and Co K-edge spectra were obtained in fluorescence mode using a multi-element silicon drift detector (SDD).

The end-station is equipped with three ionization chambers and a Lytle/SDD detector for transmission and fluorescence mode XAS. The photon flux at the sample position is approximately  $1 \times 10^{12}$  photons/sec for X-ray energies ranging at 5 keV. The acquired EXAFS (extended XAFS) data were processed according to standard procedures using the ATHENA module implemented in the IFEFFIT software package. EXAFS spectra were obtained by subtracting the post-edge background and normalizing with respect to the edge-jump step.

Electrochemical In-situ XAFS measurements were performed with a custom-designed operando electrochemical cell, which incorporated a platinum wire as the counter electrode and a leakage-free Hg/Hg<sub>2</sub>SO<sub>4</sub> electrode as the reference. The Co-Fe dual single-atom catalyst was deposited on hydrophobic carbon paper with a catalyst loading of about 5 mg/cm<sup>2</sup>, prepared by filtering a slurry of the sample in ethanol. In-situ XAFS spectra for the Co and Fe K edges were recorded at various applied voltages. Background removal and extraction of the EXAFS were carried out using the Athena software.

The collected data was analyzed via Athena and Artemis software based on the standard procedures<sup>44</sup>. The Debye-Waller factors and delta Rs are obtained based on the guessing parameters and constrained for paths. Wavelet transformation (WT) is also employed using the software package developed by Funke and Chukalina using the Morlet wavelet with  $\kappa = 10$ ,  $\sigma = 1$ <sup>45,46</sup>.

Electrochemical in situ ATR-FTIR spectra of the samples during electrocatalysis were obtained using a Linglu Instruments ECIR-II cell mounted on a Pike Veemax I ATR with a single bounce silicon crystal covered with an Au layer of 35 nm thickness in internal reflection mode. The spectra were recorded using a Thermo Nicolet Nexus 670 spectrometer. Before collecting the spectra, the electrolyte was degassed by bubbling N<sub>2</sub> in it for 30 min. A background spectrum of the working electrode was obtained at the open-circuit voltage. All spectra were presented after the baseline was deducted. The infrared data were processed using the OPUS software to obtain spectra with a better signal-to-noise ratio.

### Electrochemical measurements

The electrochemical measurements were conducted using a standard three-electrode configuration on a controlled bipotentiostat (CHI 760e, CH Instruments) and a RRDE system (Pine Research Instrumentation), where the RRDE with a glassy carbon disk (5.6 mm in diameter) and a Pt ring was employed as the working electrode<sup>47</sup>. Before testing, the 0.5 M H<sub>2</sub>SO<sub>4</sub> electrolyte was saturated with O<sub>2</sub>, and fresh acid was used for each experiment. A Pt foil counter electrode and a Hg/Hg<sub>2</sub>SO<sub>4</sub> reference electrode (calibrated against a fresh standard hydrogen electrode before use) were employed. The potential mentioned in this work was referenced to a reversible hydrogen electrode (RHE) according to the Nernst equation:

$$E_{\text{RHE}} = E_{(\text{Hg}/\text{Hg}_2\text{SO}_4)} + 0.652 + 0.059\text{pH} \quad (1)$$

To assess the stability of the catalysts, the potential was cycled between 0.6 and 1 V (vs. RHE) at a scan rate of 100 mV s<sup>-1</sup> in O<sub>2</sub>-saturated 0.5 M H<sub>2</sub>SO<sub>4</sub> with the carbon rod as the counter electrode. A homogeneous catalyst ink was prepared by ultrasonically dispersing 5 mg of catalyst powder in 470  $\mu\text{L}$  of ethanol containing 30  $\mu\text{L}$  of 5 wt% Nafion solution. 20  $\mu\text{L}$  of the ink was applied to a glassy carbon electrode by drop-casting and dried under an infrared lamp (30 min). The Staircase Cyclic Voltammetry (SCV) Parameters measurement was performed in a potential ranging from 0.05 V to 1.00 V (vs. RHE) at 900 rpm with a scan rate of 5 mV s<sup>-1</sup>, because of the relatively low activity of non-precious metal catalysts, using a low rotation speed can reduce the oxygen flow and prevent current fluctuations. The corresponding hydrogen peroxide yield (%H<sub>2</sub>O<sub>2</sub>) and the number of transferred electrons (n) can be calculated from the SCV data as the

following equations:

$$\%H_2O_2 = 200 \times \frac{I_r/N}{I_d + I_r/N} \quad (2)$$

$$n = 4 \times \frac{I_d}{I_d + I_r/N} \quad (3)$$

$I_d$  represents the absolute value of the disk current.  $I_r$  represents the absolute value of the ring current.  $N$  is the collection efficiency on the platinum ring ( $N = 0.37$ ).

The collected SCV data under various rotation speeds can be analyzed to determine the ORR kinetics using the Koutecky-Levich equation:

$$\frac{1}{j} = \frac{1}{j_L} + \frac{1}{j_K} = \frac{1}{B\omega^{1/2}} + \frac{1}{j_K} \quad (4)$$

$$B = 0.62nFC_0(D_0)^{2/3}\nu^{-1/6} \quad (5)$$

$j$ ,  $j_K$ , and  $j_L$  represent the measured current density, the kinetic current density, and the diffusion-limiting current density, respectively.  $\omega$  represents the angular velocity.  $F$  represents the Faraday constant ( $96485 \text{ C mol}^{-1}$ ).  $C_0$  represents the bulk concentration of oxygen in the electrolyte ( $1.2 \times 10^{-6} \text{ mol cm}^{-3}$ ).  $D_0$  represents the oxygen diffusion coefficient in the electrolyte ( $1.9 \times 10^{-5} \text{ cm}^2 \text{ s}^{-1}$ ).  $\nu$  represents the kinematic viscosity of the electrolyte ( $0.01 \text{ cm}^2 \text{ s}^{-1}$ ).

Electrochemical active surface area of the catalysts was estimated from the electrochemical double-layer capacitance ( $C_{dl}$ ) in non-faradaic potential regions of the catalytic surface using the following equation:

$$C_{dl} = \Delta J / 2\nu \quad (6)$$

$$ECSA = C_{dl} / C_s \quad (7)$$

where the current density difference ( $\Delta J = J_{anodic} - J_{cathodic}$ ) at 0.48 V vs. RHE was systematically plotted against scan rate ( $\nu$ ) and the  $C_{dl}$  was obtained from the CVs that were dependent on the scan rate, recorded in the non-Faradaic region between 0.40 and 0.59 V vs. RHE in 0.5 M  $H_2SO_4$ , utilizing scan rates of 10, 20, 30, 40, and 50  $\text{mV s}^{-1}$ . This analysis revealed a linear correlation, where the slope of the fitted line corresponds to twice the geometric double-layer capacitance ( $C_{dl}$ ). Since the double-layer capacitance directly reflects the interface characteristics between the electrode and electrolyte, this derived  $C_{dl}$  value serves as a critical proportional indicator of the material's electrochemically accessible surface area. The double-layer capacitance ( $C_s$ ) used is 0.02  $\text{mF cm}^{-2}$  here.

### MEA tests

The cathode electrode was prepared via the gas diffusion electrode (GDE) method. Catalyst inks were prepared by mixing the catalysts and ionomer in an isopropanol-water solution with a volume ratio of 1:1. The solid content was 6%, the ionomer-to-catalyst ratio was kept at 0.7, and the ink was subjected to sonication for 1 h. The catalyst inks were then brushed on a piece of gas diffusion layer ( $5 \text{ cm}^2$ ) with a loading of  $3.5 \text{ mg cm}^{-2}$  as the cathode. The anode electrode was prepared via the catalyst coated membrane (CCM) method. Commercial Pt/C (60 wt%) was deposited on a proton exchange membrane (Gore M765.08) with a loading of  $0.1 \text{ mg}_{Pt} \text{ cm}^{-2}$  as the anode. The MEA was fabricated by pressing the as-prepared cathode and anode onto the two sides of a proton exchange membrane (Gore M765.08) at  $130 \text{ }^\circ\text{C}$  for 2 min, under 2 MPa. The MEA was tested in a single-cell and condition-controlled fuel-cell test station (Scribner 850e, Scribner Associates). Operating

conditions for the PEMFC tests included: a cell temperature of  $80 \text{ }^\circ\text{C}$ , reactant gas flow rates ( $H_2$ :  $0.5 \text{ L min}^{-1}$ ,  $O_2$ :  $0.5 \text{ L min}^{-1}$ , air:  $2 \text{ L min}^{-1}$ ), and 100% relative humidity<sup>17</sup>. The MEA employed a Pt/C cathode ( $0.05 \text{ mg}_{Pt} \text{ cm}^{-2}$  loading). Fuel cell polarization was measured under voltage control at 200 kPa total pressure. Durability tests were carried out in  $H_2$  (200 sccm)/ $N_2$  (75 sccm) using a square wave cycling protocol (0.6 V for 3 s, 0.90 V for 3 s,  $80 \text{ }^\circ\text{C}$ , 100% RH, and 0 bar). EIS was conducted at 0.60 V under  $H_2$ -air conditions over frequencies ranging from 10,000 Hz to 0.1 Hz.

### DFT calculations

All the spin-polarized density-functional theory (DFT)<sup>48,49</sup> calculations were carried out using the Vienna Ab initio Simulation Package<sup>50,51</sup> software. The exchange-correlation functional adopted is the Perdew-Burke-Ernzerhof<sup>52</sup> generalized gradient approximation. The projector augmented-wave<sup>53</sup> method is used with a cutoff energy of 520 eV. A  $6 \times 6$  supercell of graphene layer was employed to model our nitrogen-doped electrocatalysts, denoted as Fe-NC, FeCo-NC, and FeCo-NC-OH, with a vacuum region of  $15 \text{ \AA}$  to avoid imaginary interactions between periodic images. To ensure the convergence of calculations, care was taken to choose the  $k$ -point mesh in the reciprocal space. A  $4 \times 4 \times 1$  Monkhorst-Pack<sup>54</sup>  $k$ -point grid was used for the geometry optimization, while a denser  $k$ -grid of  $8 \times 8 \times 1$  was employed for the electronic-structure calculations. The convergence criteria were  $10^{-6} \text{ eV}$  for the total energy and  $0.02 \text{ eV/\AA}$  for the forces. Frequency analysis was performed to obtain accurate free energy profiles, followed by zero-point vibrational corrections. The Lobster code<sup>55</sup> was employed to evaluate the Crystal Orbital Hamilton Population (COHP).

In this work, the change in Gibbs free energy ( $\Delta G$ ) is expressed as:

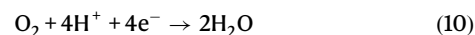
$$\Delta G = E + ZPE - T\Delta S + \Delta G_U + \Delta G_{pH} \quad (8)$$

where  $E$  is the total energy obtained from the DFT calculations, and ZPE corresponds to the zero-point energy (ZPE) contribution to the total energy.  $T$  and  $\Delta S$  refer to the temperature (298.15 K) and the change of entropy, respectively.  $\Delta G_U$  and  $\Delta G_{pH}$  represent the contributions of applied potential and  $H^+$  concentration for the free energies, and the latter can be computed via

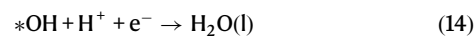
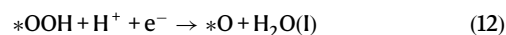
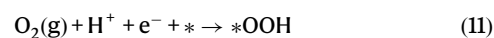
$$\Delta G_{pH} = -k_B T \ln[H^+] = pH \times k_B T \times \ln 10 \quad (9)$$

where  $k_B$  is the Boltzmann constant and  $[H^+]$  represents the concentration of hydrogen ions. Under standard conditions, when the temperature is 298.15 K and the concentration of hydrogen ions is 1 mol/L,  $pH = 0$ , and  $\Delta G_{pH} = 0$ . Compared with the standard hydrogen electrode (SHE),  $\Delta G_U = 0$ .

The overall reaction scheme of the ORR is given by



The ORR four-electron pathway under acidic conditions can be generally written as the following elementary steps:



where  $*$  stands for an active site on the catalytic surface, (l) and (g) refer to liquid and gas phases, respectively.

The Gibbs free energies of (9)–(12) for ORR can be calculated using the following equations:

$$\Delta G_1 = \Delta G_{*OOH} - 4.92 \quad (15)$$

$$\Delta G_2 = \Delta G_{*O} - \Delta G_{*OOH} \quad (16)$$

$$\Delta G_3 = \Delta G_{*OH} - \Delta G_{*O} \quad (17)$$

$$\Delta G_4 = -\Delta G_{*OH} \quad (18)$$

Then, the overpotential (V vs. SHE) is obtained by

$$\eta^{ORR} = \frac{\max[\Delta G_1, \Delta G_2, \Delta G_3, \Delta G_4]}{e} + 1.23V \quad (19)$$

The lower value of  $\eta$  is, the better predicted ORR activity is.

To measure the strength of the oxygenated intermediates adsorption on the catalyst surface, the adsorption energy ( $E_{ads}$ ) is calculated by

$$E_{ads} = E_{mole}^{surf} - E_{surf} - E_{mole} \quad (20)$$

$E_{mole}^{surf}$ ,  $E_{surf}$  and  $E_{mole}$  represent the total energies of the oxygenated intermediates adsorbed on the catalyst surface, pure catalyst surface, and the adsorbent molecules, respectively. The magnitude of adsorption energy is inversely proportional to the strength of adsorption. A more negative value of  $E_{ads}$  indicates that the oxygenated species is more strongly adsorbed on the catalyst surface.

According to the  $d$ -band center model of Hammer-Nørskov<sup>56</sup>, the  $d$ -band center can be considered as an indicator of the catalytic activity of TM. This model suggests the change of the adsorption energy can be correlated to the shift of the  $d$ -band center. More specifically, the upshift of the  $d$ -band center offers a way of increasing the number of empty anti-bonding states, yielding to a stronger adsorption, and vice versa.

## Data availability

All data supporting the findings of this study are available within the paper and its supplementary information files or from the corresponding authors upon request. Source data are provided with this paper.

## References

- Wong, M. K. et al. Leveraging dual-atom catalysts for electrocatalysis revitalization: exploring the structure-performance correlation. *Adv. Energy Mater.* **14**, 2303281 (2024).
- Zhang, W. et al. Emerging dual-atomic-site catalysts for efficient energy catalysis. *Adv. Mater.* **33**, 2102576 (2021).
- Yuan, L.-J. et al. Strategies and mechanism for enhancing intrinsic activity of metal-nitrogen-carbon catalysts in electrocatalytic reactions. *Renewables* **1**, 514–540 (2023).
- Yuan, L. J. et al. Electrocatalysis mechanism and structure-activity relationship of atomically dispersed metal-nitrogen-carbon catalysts for electrocatalytic reactions. *Small Methods* **7**, 2201524 (2023).
- Wang, X. et al. Single-atom engineering to ignite 2D transition metal dichalcogenide based catalysis: fundamentals, progress, and beyond. *Chem. Rev.* **122**, 1273–1348 (2021).
- Shahzad, A. et al. Cobalt containing bimetallic ZIFs and their derivatives as OER electrocatalysts: A critical review. *Coord. Chem. Rev.* **477**, 214925 (2023).
- Gao, Y. et al. Microenvironment engineering of single/dual-atom catalysts for electrocatalytic application. *Adv. Mater.* **35**, 2209654 (2023).
- Huang, S. et al. Asymmetric microenvironment tailoring strategies of atomically dispersed dual-site catalysts for oxygen reduction and CO<sub>2</sub> reduction reactions. *Adv. Mater.* **36**, 2407974 (2024).
- Meng, C. et al. Synergy of atomically dispersed Co-Fe pairs in nanoconfined catalytic membranes enabling efficient water purification. *Appl. Catal. B Environ. Energy* **359**, 124449 (2024).
- Liu, L. et al. Insight into synergy for oxygen reduction electrocatalysis of iron-nitrogen-carbon. *Chem* **10**, 1994–2030 (2024).
- Zhang, W. et al. Fe-based dual-atom catalysts for the oxygen reduction reaction. *J. Mater. Chem. A* **12**, 87–112 (2024).
- Zhang, Y.-X. et al. General synthesis of a diatomic catalyst library via a macrocyclic precursor-mediated approach. *J. Am. Chem. Soc.* **145**, 4819–4827 (2023).
- Zhang, S. et al. Atomically dispersed bimetallic Fe-Co electrocatalysts for green production of ammonia. *Nat. Sustain.* **6**, 169–179 (2022).
- Li, Y. et al. Precisely constructing charge-asymmetric dual-atom Fe sites supported on hollow porous carbon spheres for efficient oxygen reduction. *Energy Environ. Sci.* **17**, 4646–4657 (2024).
- Liu, F. et al. Fe/Co dual metal catalysts modulated by S-ligands for efficient acidic oxygen reduction in PEMFC. *Sci. Adv.* **9**, eadg0366 (2023).
- Tang, B. et al. A Janus dual-atom catalyst for electrocatalytic oxygen reduction and evolution. *Nat. Synth.* **3**, 878–890 (2024).
- Zhang, N. et al. High-density planar-like Fe<sub>2</sub>N<sub>6</sub> structure catalyzes efficient oxygen reduction. *Matter* **3**, 509–521 (2020).
- Li, L. et al. Tailoring atomic strain environment for high-performance acidic oxygen reduction by Fe-Ru dual atoms communicative effect. *Matter* **7**, 1517–1532 (2024).
- Guo, P. et al. Breaking Sabatier's vertex via switching the oxygen adsorption configuration and reaction pathway on dual active sites for acidic oxygen reduction. *Energy Environ. Sci.* **17**, 3077–3087 (2024).
- Du, J. et al. CoIn dual-atom catalyst for hydrogen peroxide production via oxygen reduction reaction in acid. *Nat. Commun.* **14**, 4766 (2023).
- Ooka, H. et al. The sabatier principle in electrocatalysis: basics, limitations, and extensions. *Front. Energy Res.* **9**, 654460 (2021).
- He, Y. et al. Atomically dispersed metal-nitrogen-carbon catalysts for fuel cells: advances in catalyst design, electrode performance, and durability improvement. *Chem. Soc. Rev.* **49**, 3484–3524 (2020).
- Li, R. et al. Superiority of dual-atom catalysts in electrocatalysis: one step further than single-atom catalysts. *Adv. Energy Mater.* **12**, 2103564 (2022).
- Jiang, M. et al. Rationalization on high-loading iron and cobalt dual metal single atoms and mechanistic insight into the oxygen reduction reaction. *Nano Energy* **93**, 106793 (2022).
- Wang, J. et al. Design of N-coordinated dual-metal sites: a stable and active Pt-free catalyst for acidic oxygen reduction reaction. *J. Am. Chem. Soc.* **139**, 17281–17284 (2017).
- Xiao, M. et al. Climbing the apex of the ORR volcano plot via binuclear site construction: electronic and geometric engineering. *J. Am. Chem. Soc.* **141**, 17763–17770 (2019).
- Vafaezadeh, M. et al. Task-specific janus materials in heterogeneous catalysis. *Angew. Chem. Int. Ed.* **61**, e202206403 (2022).
- Wang, B. et al. A general metal ion recognition strategy to mediate dual-atomic-site catalysts. *J. Am. Chem. Soc.* **146**, 24945–24955 (2024).
- Zhu, X. et al. Activity origin and design principles for oxygen reduction on dual-metal-site catalysts: a combined density

- functional theory and machine learning study. *J. Phys. Chem. Lett.* **10**, 7760–7766 (2019).
30. Liu, J. et al. Understanding the Pathway switch of the oxygen reduction reaction from single- to double-/triple-atom catalysts: a dual channel for electron acceptance-backdonation. *JACS Au*. **3**, 3031–3044 (2023).
  31. Hu, R. et al. Role of active sites in N-coordinated Fe-Co dual-metal doped graphene for oxygen reduction and evolution reactions: A theoretical insight. *Appl. Surf. Sci.* **525**, 146588 (2020).
  32. Yuan, L. J. et al. d-orbital electron delocalization realized by axial Fe<sub>4</sub>C atomic clusters delivers high-performance Fe-N-C catalysts for oxygen reduction reaction. *Adv. Mater.* **35**, 2305945 (2023).
  33. Sun, K. et al. Co(CN)<sub>3</sub> catalysts with well-defined coordination structure for the oxygen reduction reaction. *Nat. Catal.* **6**, 1164–1173 (2023).
  34. Hao, B. et al. Concentration polarization induced phase rigidification in ultralow salt colloid chemistry to stabilize cryogenic Zn batteries. *Nat. Commun.* **15**, 9465 (2024).
  35. Balmer, J. A. et al. Unexpected facile redistribution of adsorbed silica nanoparticles between latexes. *J. Am. Chem. Soc.* **132**, 2166–2168 (2010).
  36. Serikov, V. V. et al. NMR and Mössbauer study of peculiarities of the structure formation in Fe-Co alloys. *Phys. Met. Metall.* **118**, 1040–1047 (2017).
  37. Fock, J. et al. On the interpretation of Mössbauer spectra of magnetic nanoparticles. *J. Magn. Magn. Mater.* **445**, 11–21 (2018).
  38. Germov, A. Y. et al. NMR and Mossbauer studies of core-shell FeCo@C ferromagnetic nanoparticles near the superparamagnetic transition. *J. Magn. Magn. Mater.* **588**, 171391 (2023).
  39. An, S. Y. Mössbauer and magnetic properties of graphene oxides coatings on Fe and FeCo powders for high frequency applications. *J. Radioanal. Nucl. Chem.* **332**, 5105–5112 (2023).
  40. Li, J. et al. Identification of durable and non-durable FeN<sub>x</sub> sites in Fe-N-C materials for proton exchange membrane fuel cells. *Nat. Catal.* **4**, 10–19 (2020).
  41. Zhao, K.-M. et al. Identifying high-spin hydroxyl-coordinated Fe<sup>3+</sup>N<sub>4</sub> as the active centre for acidic oxygen reduction using molecular model catalysts. *Nat. Catal.* **8**, 422–435 (2025).
  42. Iwasawa Y. et al. *XAFS Techniques for Catalysts, Nanomaterials, and Surfaces* (Springer International Publishing Switzerland, 2017).
  43. Lu, R. et al. Establishing a theoretical insight for penta-coordinated iron-nitrogen-carbon catalysts toward oxygen reaction. *Nano Res.* **15**, 6067–6075 (2022).
  44. Ravel, B. et al. ATHENA, ARTEMIS, HEPHAESTUS: data analysis for X-ray absorption spectroscopy using IFEFFIT. *J. Synchrotron Radiat.* **12**, 537–541 (2005).
  45. Funke, H. et al. Wavelet analysis of extended X-ray absorption fine structure data. *Phys. Rev. B.* **71**, 094110 (2005).
  46. Funke, H. et al. A new FEFF-based wavelet for EXAFS data analysis. *J. Synchrotron Radiat.* **14**, 426–432 (2007).
  47. Liu, Y. et al. Physical and chemical dual-induced growth optimizing the size of porous Fe-N-C catalysts to achieve high accessibility of active sites. *Appl. Surf. Sci.* **708**, 163699 (2025).
  48. Kohn, W. et al. Self-consistent equations including exchange and correlation effects. *Phys. Rev.* **140**, A1133–A1138 (1965).
  49. Hohenberg, P. et al. Inhomogeneous electron gas. *Phys. Rev.* **136**, B864–B871 (1964).
  50. Kresse, G. et al. Efficiency of ab-initio total energy calculations for metals and semiconductors using a plane-wave basis set. *Comput. Mater. Sci.* **6**, 15–50 (1996).
  51. Kresse, G. et al. Efficient iterative schemes for ab initio total-energy calculations using a plane-wave basis set. *Phys. Rev. B.* **54**, 11169–11186 (1996).
  52. Perdew, J. P. et al. Generalized gradient approximation made simple. *Phys. Rev. Lett.* **77**, 3865–3868 (1996).
  53. Kresse, G. et al. From ultrasoft pseudopotentials to the projector augmented-wave method. *Phys. Rev. B.* **59**, 1758–1775 (1999).
  54. Monkhorst, H. J. et al. Special points for Brillouin-zone integrations. *Phys. Rev. B.* **13**, 5188–5192 (1976).
  55. Deringer, V. L. et al. Crystal orbital Hamilton population (COHP) analysis as projected from plane-wave basis sets. *J. Phys. Chem. A.* **115**, 5461–5466 (2011).
  56. Ruban, A. et al. Surface electronic structure and reactivity of transition and noble metals. *J. Mol. Catal. A Chem.* **115**, 421–429 (1997).

## Acknowledgements

This work was supported by the National Natural Science Foundation of China (Grant No. 52472226, 22075062 and U23A20573), the High-Level Professional Team in Shenzhen (KQTD20210811090045006), the Shenzhen Science and Technology Program (No. KJZD20240903095610014, KJZD20240903095712017 and JCYJ20210324120400002), the Key Research and Development Program of Shandong Province (2022CXGC010305), Heilongjiang Touyan Team (Grant No. HITTY-20190033), the Fundamental Research Funds for the Central Universities (Grant No. FRFCU5710051922), and Guangdong Basic and Applied Basic Research Foundation (No. 2023B1515120022, 2022B1515120001). H.-T.W. acknowledges support from the National Science and Technology Council (NSTC), Taiwan (Grant no. 112-2112-M-032-017-MY2). The ex/in-situ XAFS spectra obtained from beamline TPS 32A at NSRRC are appreciated. The authors would also like to acknowledge the valuable assistance received from the Electron Microscope Center of Shenzhen University and the Instrumental Analysis Center of Shenzhen University.

## Author contributions

L.-J.Y. designed and completed the experimental work and article writing. Z.-Y.M. led the theoretical calculations. C.-F.L., Y.-R.L., and H.-T.W. carried out the ex-situ and in-situ XAS characterizations. Q.L. W.G. performed the experiments. M.-J.Y. carried out the TEM and HAADF-STEM characterizations. L.-X.S., Z.-G.Z., Y.-Z.L., and L.-S.Z. are responsible for the testing of the membrane electrode assembly. W.-L.F., H.-T.W., G.-X.Z., and X.-L.S. provided comments on the experiments and revisions to the article. H.-T.W., G.-X.Z., X.-L.S., and Z.-B.W. reviewed and corrected the manuscript. All authors discussed the results and commented on the manuscript.

## Competing interests

The authors declare no competing interests.

## Additional information

**Supplementary information** The online version contains supplementary material available at <https://doi.org/10.1038/s41467-025-62728-4>.

**Correspondence** and requests for materials should be addressed to Xu-Lei Sui, Hsiao-Tsu Wang, Guo-Xu Zhang or Zhen-Bo Wang.

**Peer review information** *Nature Communications* thanks the anonymous reviewer(s) for their contribution to the peer review of this work. A peer review file is available.

**Reprints and permissions information** is available at <http://www.nature.com/reprints>

**Publisher's note** Springer Nature remains neutral with regard to jurisdictional claims in published maps and institutional affiliations.

**Open Access** This article is licensed under a Creative Commons Attribution-NonCommercial-NoDerivatives 4.0 International License, which permits any non-commercial use, sharing, distribution and reproduction in any medium or format, as long as you give appropriate credit to the original author(s) and the source, provide a link to the Creative Commons licence, and indicate if you modified the licensed material. You do not have permission under this licence to share adapted material derived from this article or parts of it. The images or other third party material in this article are included in the article's Creative Commons licence, unless indicated otherwise in a credit line to the material. If material is not included in the article's Creative Commons licence and your intended use is not permitted by statutory regulation or exceeds the permitted use, you will need to obtain permission directly from the copyright holder. To view a copy of this licence, visit <http://creativecommons.org/licenses/by-nc-nd/4.0/>.

© The Author(s) 2025